Journal of Fluids and Structures 18 (2003) 287–304

JOURNAL OF FLUIDS AND STRUCTURES

www.elsevier.nl/locate/jnlabr/yjfls

Mesh shape preservation for flow-induced vibration problems

R.M.C. So[a,*], Y. Liu[a], Y.G. Lai[b]

[a] *Department of Mechanical Engineering, The Hong Kong Polytechnic University, Hung Hom, Kowloon, Hong Kong*
[b] *Institute of Hydraulic Research, University of Iowa, Iowa City, IA 52242, USA*

Received 25 October 2001; accepted 19 May 2003

Abstract

This paper describes a numerical technique that can prevent the mesh from severe distortion in flow-induced vibration calculations. An orthogonal transformed space that is related to the physical space through a Laplacian equation is introduced. At each time step, the mesh may deform significantly in the physical space due to structural vibration, but the mesh nodal value in the transformed space remains constant. As long as the coordinates in the physical space can be adjusted to render the transformed space independent of time, the mesh shape in the physical space is preserved, even though the mesh area may enlarge or reduce significantly. For simplicity, a two-dimensional flow-induced vibration problem is used to illustrate this method. Two side-by-side elastic cylinders in a cross flow are considered. The Reynolds number is fixed at 200, corresponding to a laminar wake. The mass ratio is chosen to be small so that large displacements of the cylinders can be realized. Predictions with and without mesh preservation are compared. The difference between the two results could be as large as 25% in the prediction of the mean transverse displacements of the cylinders. The method could be extended to three-dimensional flow-induced vibration problems without much difficulty.

1. Introduction

Offshore drilling and production systems, most notably tension leg platforms (TLPs), have become increasingly popular for the exploration and production of oil fields in deep water (1000–3000 m). Tension leg platforms contain a large number of risers and tendons that span almost the entire water depth. These flexible cylinders are subjected to a combined loading of waves and currents, and are highly susceptible to vortex-induced vibrations. In certain instances, fluid–structure coupling could give rise to a resonant condition; thus yielding excessive vibration amplitudes that lead to structural failure. Consequently, the prediction and control of flow-induced vibrations, particularly with the design of offshore risers and spars, are of critical concern to the offshore oil industry.

One approach to tackle the problem of flow-induced vibrations of offshore risers and spars in close proximity is to develop an understanding of the interactions between the near-wake flow and the structural dynamics. The problem could be idealized by considering multiple cylinders in close proximity with each other freely vibrating in a cross-flow. Understanding of the physics could be gained through experimental investigations, or by numerically simulating the flow around some relatively simple arrangements of bluff bodies. The experimental approach could be very effective when the vibration amplitudes of the structures are not excessively large, say within one hydraulic diameter of the structures. When the vibration amplitudes become too large, the errors involved in their measurements could be unacceptable if optical techniques are used to measure vibration amplitude directly. These errors stem mainly from the large curvature of the structure and the necessity to maintain accuracy in the focusing of the optical beam (So et al.,

*Corresponding author. Fax: +852-2365-4703.
E-mail address: mmmcso@polyu.edu.hk (R.M.C. So).

0889-9746/$ - see front matter © 2003 Elsevier Ltd. All rights reserved.
doi:10.1016/j.jfluidstructs.2003.05.002

2000). Other indirect methods, such as strain gauges and force cells, could be used to measure the strains and the forces though. However, these alternative methods could lead to other problems not found in the use of optical techniques (So and Savkar, 1981). On the other hand, large vibration amplitudes would give rise to excessive deformation of the computational grid in the case of numerical simulations. Very large grid deformation would lead to errors in the computation of the flow behavior near the surface of the structures and estimate of the surface pressure and induced forces. These errors could contribute to incorrect predictions of the structural dynamics.

In the past, fundamental understanding of the physics of fluid–structure interactions has been gained by considering a single cylinder in a cross flow with small to medium vibration amplitude. There are numerous experimental studies devoted to free and forced vibration of a single cylinder. Among the more notable studies on free vibration are the work of Griffin et al. (1973), Griffin and Koopmann (1977), Obasaju et al. (1990), Sarpkaya (1995), Khalak and Williamson (1996), and So et al. (2000). As for forced vibration, the work of Bearman (1988), Williamson and Roshko (1988), Griffin and Hall (1991), and Gopalkrishnan et al. (1994) can be mentioned. Through these studies and many more, the phenomena of synchronization with the vortex-shedding frequency for free vibration and the lock-on behavior with the imposed frequency for forced vibration were discovered and the physics associated with them were understood.

Various numerical techniques have been used to simulate this class of problems. These include grid-free methods, such as the surface vorticity method (Lewis, 1991), and grid methods, such as finite-element methods (Mittal and Kumar, 1999; Mendes and Branco, 1999; So et al., 2001) and direct numerical simulations (Newman and Karniadakis, 1997; Evangelinos and Karniadakis, 1999; Evangelinos et al., 2000). The numerical simulations were able to replicate the observed phenomena for free and forced vibration of a single cylinder. In this simple case, even a large vibration amplitude would not lead to excessive errors in the computation of the surface pressure and induced forces, and hence the cylinder dynamics. The reason is that grid deformation is not large, because the problem could be formulated by attaching the coordinate system to the moving cylinder. This, however, is not applicable for multiple cylinders in a cross flow. As a result, the grids in the confined space between two cylinders could be grossly deformed depending on the vibration amplitudes (Liu et al., 2001). It would seem that the grid-free (vortex) methods would be most appropriate for flow-induced vibration problems with multiple structures. Unfortunately, at present, they are limited to two-dimensional (2-D) flows and cannot be easily extended to 3-D problems.

The relatively simple case of two side-by-side cylinders in a cross flow has been numerically investigated by a number of researchers. For example, Stansby (1981) studied this problem using an essentially inviscid discrete-vortex method, but Chang and Song (1990) used a blending technique comprised of a finite-element method in the vicinity of the bodies and a finite-difference method for the rest of the flow field. On the other hand, Tezduyar et al. (1990) used a finite element formulation with the streamline-upwind/Petrov–Galerkin method (SUPG), Meneghini et al. (2001) used a fractional step method with a Galerkin finite element formulation, while Slaouti and Stansby (1992) adopted a random-vortex method. Most of these numerical studies have only considered the rigid cylinder case, and the interactions of fluid and elastic structures are typically ignored due to numerical complexities. The case of two flexible cylinders was treated by Liu et al. (2001). In their calculations, the coordinate system has to be attached to an inertial frame and cylinder vibrations have to be accounted for by mesh deformation. Therefore, they have to limit their investigation to cylinders with small to moderate vibration amplitudes. Otherwise, the numerical errors could be excessive. These numerical studies were able to replicate the near-wake behavior for the rigid as well as the flexible cylinder case. They include the various flow regimes resulting from different T/D ratios as observed in experimental investigations (Spivack, 1946; Bearman and Wadcock, 1973; Williamson, 1985; Bearman, 1995; Sumner et al., 1997, 1999; Paidoussis, 1998; Zhou et al., 2001). Here, T is the spacing between cylinder diameters and D is the cylinder diameter.

For offshore applications, the vibration amplitudes of a single flexible cylinder in waves can be as large as 5–10D in the inline direction and 1–2D in the transverse direction (Duggal and Niedzwecki, 1995). To simulate the fluid–structure interaction correctly, structural vibration has to be accounted for by mesh deformation. There are several numerical techniques to tackle this mesh movement. The arbitrary Lagrangian–Eulerian (ALE) method was introduced by Hirt et al. (1974) in association with a finite-difference technique. The same ALE method was later developed in association with a finite-element approach (Donea et al., 1982; Ramaswamy and Kawahara, 1987; Nomura and Hughes, 1992; Farhat et al., 1995; Wei et al., 1995). Besides ALE, other methods, using different kinds of grid remeshing, can also be found in the literature for the analysis of fluid–structure interactions (Hurlbut et al., 1982; Chilukuri, 1987; Lecointe and Piquet, 1989; Mittal and Tezduyar, 1992; Zhang and Dalton, 1997; Yang et al., 1997; Liu et al., 2001). For example, Liu et al. (2001) calculated the fluid–structure interaction for the case of two side-by-side elastic cylinders in a cross flow. They accounted for the arbitrary motions of the two cylinders by introducing a moving mesh technique. Even though Laplacian interpolation was used to reduce mesh deformation, the mesh still distorted significantly due to the rather large vibration displacement, with a peak-to-peak value of about 1D. The distortion is especially substantial when the two cylinders move towards each other, thus leading to a severe squeeze of the mesh between the cylinders. Typical finite element methods use linear or quadratic shape functions to define the problem within each element. For

large deformation problems, the elements must be very small to accurately predict the gradient. Consequently, it could lead to serious mesh distortion and mesh entanglements, which render the finite-element method invalid.

All these techniques require continuous remeshing if they are used to treat fluid–structure interaction problems with large deformation. If this tedious step is to be avoided, a technique to preserve the mesh shape whereby the numerical calculations can be carried out accurately will have to be developed. The objective of the present study is to do just that, i.e., to develop a numerical technique that can preserve the mesh shape even though the mesh area may enlarge or reduce significantly from one time step to the next. A method that has been successfully developed by Hui et al. (1999) to treat two-dimensional Euler equations, where discontinuities such as shocks, material interfaces, etc., exist in the flow, is used to help guide the development of the present method. The formulation is first given assuming a 3-D problem. However, as a first attempt, only a 2-D problem is used to illustrate the implementation of the method in a numerical simulation. Its extension to 3-D problems is the topic of a separate investigation.

2. Numerical method

Three elements are of primary importance to the numerical simulation of flow-induced vibration problems. These are the flow field calculation, the structural dynamics evaluation and the fluid–structure interaction resolution. Various finite-difference and finite-element methods are available for the calculation of the flow field. If a N-degree-of-freedom or an Euler–Bernoulli beam model were used to resolve the structural vibrations, standard numerical techniques are also available. Thus, the correct simulation of flow-induced vibration hinges on how accurately the fluid–structure interaction can be resolved. This is where the complications come in for flow-induced vibration of multiple structures with large vibration amplitudes. The finite-difference or finite-element grid would be seriously deformed in the space between structures and this could lead to excessively large errors in the calculation of the flow field, the surface forces and the structural responses. Standard techniques are available for the first two parts (see, e.g., Wang et al., 2001; Liu et al., 2001). Therefore, this paper concentrates on the third part, to resolve correctly the fluid–structure interaction. A method to preserve the mesh shape irrespective of the grid deformation is proposed. To illustrate the implementation of the method in a numerical simulation, two side-by-side elastic cylinders in a 2-D cross flow are considered. For the sake of completeness, a brief description of the first two parts for this relatively simple problem is given below, while a detailed discussion of the mesh shape preservation method is presented in Section 3.

2.1. Flow calculations

A schematic view of the problem is shown in Fig. 1. Two side-by-side elastic cylinders with fixed support at both ends are placed in a 2-D cross flow with a free-stream velocity U_∞. The computational domain is a $25D \times 16D$ rectangular region, the upstream length is about $5D$, while the downstream length is $20D$, and the two cylinders are located symmetrically about the center-line. The calculation using this domain was compared with that using a larger domain of $50D \times 20D$. The calculated mean drag of these two cases agrees to within 1% of each other. Even though practical problems are usually turbulent and the Reynolds numbers (Re) are very high, in the context of this work, a consideration of laminar flow with moderate Re is sufficient to illustrate the mesh shape preservation technique. For the case of laminar, incompressible flows, the governing equations are

$$\nabla \cdot \mathbf{u} = 0, \tag{1}$$

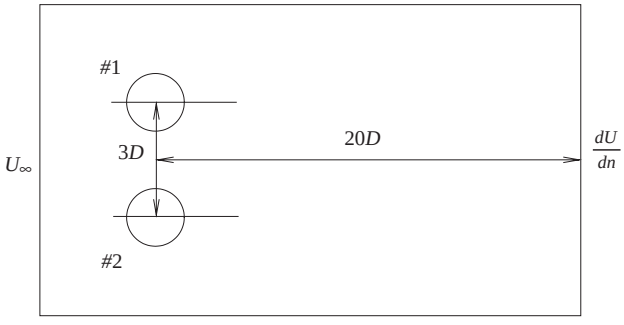

Fig. 1. Schematic illustration of the problem.

$$\frac{\partial \mathbf{u}}{\partial \tau} + \mathbf{u} \cdot \nabla \mathbf{u} = -\nabla p + \frac{1}{\mathrm{Re}} \nabla^2 \mathbf{u}. \tag{2}$$

In these equations, $\nabla = \mathbf{i}\partial/\partial x + \mathbf{j}\partial/\partial y$ is the differential operator, $\mathbf{x} = (\mathbf{i}x + \mathbf{j}y)$ is the Cartesian position vector, $\mathbf{u} = (\mathbf{i}u + \mathbf{j}v)$ is the velocity vector, $\mathbf{i}$ and $\mathbf{j}$ are unit vectors along the x- and y-axis, respectively, p is the static pressure, τ is time and $\mathrm{Re} = U_\infty D/v$ is the flow Reynolds number. It should be pointed out that, for a single structure, the coordinate system can be attached to the structure, while for multiple structures the coordinate system is attached to a reference frame, such as the calculation domain. All the variables in the equations are dimensionless. They are defined with respect to the physical variables (denoted here by the superscript *, except for time t) by $\mathbf{x} = \mathbf{x}^*/D, \mathbf{u} = \mathbf{u}^*/U_\infty, p = (p^* - p_\infty)/\rho U_\infty^2$ and $\tau = tU_\infty/D$. To complete the formulation, the boundary conditions are given as

(i) At the upstream far field, domain top boundary and domain bottom boundary,

$$u = \mathbf{1} \text{ and } v = 0. \tag{3}$$

(ii) At the downstream far field,

$$\frac{\partial u}{\partial n} = 0, \tag{4}$$

where n denotes the normal direction of the curvilinear coordinates attached to the boundary.

(iii) At the surface of the cylinders,

$$\mathbf{u} \cdot \mathbf{n} = \mathbf{u}_{cy} \cdot \mathbf{n}, \tag{5}$$

where $\mathbf{u}_{cy}$ is the velocity of the cylinders and $\mathbf{n}$ is the unit normal vector.

The Navier–Stokes equations are solved using a finite-element method (FEM) and the nonlinear coupling terms in the equations are treated separately, at different fractional time steps, by an operator splitting time stepping method. The method is suitable for both steady and transient problems and can readily be extended to include extra equations describing additional physical effects, such as the effects of cylinder motions on the flow field and vice versa. A detailed discussion of the numerical technique and validation of the program have been presented elsewhere (Liu et al., 2001).

Since the boundary layer is expected to be thin near the cylinder, a fine mesh is concentrated near the cylinder surface. The number of panels is 220, the number of nodes is about 63 589, and the number of elements is numerically determined to be about 31 589. This is adequate to resolve the velocity and the boundary layer. These numbers are determined by using different meshes, from coarser to progressively finer meshes, until the drag coefficient is mesh-convergent to within a prescribed tolerance of about 0.5%.

2.2. Cylinder dynamics

Wang et al. (2001) have shown that the Euler–Bernoulli beam theory can be used to calculate the structural dynamics in flow-induced vibration problems with not much additional difficulties compared to an N-degree-of-freedom model. On the other hand, So et al. (2001) have demonstrated that a two-degree-of-freedom (2d.o.f.) model yields results that are essentially the same as those obtained from the beam model at mid-span of the structure. As a first attempt, the mesh shape preservation technique is demonstrated by choosing a dynamics model that is relatively simple. Therefore, for the sake of simplicity, the present attempt chooses a 2d.o.f. model for the cylinder dynamics. The circular cylinders are fixed at both ends. Thus, the dynamic response of each cylinder is described by the 2d.o.f. equation,

$$\frac{\mathrm{d}^2 \boldsymbol{\chi}}{\mathrm{d}t^2} + \frac{4\pi\zeta_s}{U_r} \frac{\mathrm{d}\boldsymbol{\chi}}{\mathrm{d}t} + \left(\frac{2\pi}{U_r}\right)^2 \boldsymbol{\chi} = \frac{\mathbf{C}_f}{2M_r}, \tag{6}$$

where $\boldsymbol{\chi} = X\mathbf{i} + Y\mathbf{j}$, X and Y denote the instantaneous displacements of the cylinders in the x- and y-direction, respectively, ζ_s is the dimensionless structural damping coefficient, $M_r = M/(\rho D^2)$ is the mass ratio, ρ is the fluid density, M is the mass per unit length of the cylinder, $\mathbf{C}_f = \mathrm{C}_D\mathbf{i} + \mathrm{C}_L\mathbf{j}$ is the force coefficient, defined as $\mathbf{C}_f = 2\mathbf{F}/\rho U_\infty{}^2 D$, $\mathbf{F}$ is the instantaneous vortex-induced force vector, and U_r is the reduced velocity. The drag and lift coefficient C_D and C_L, respectively, are defined similarly to $\mathbf{C}_f$ and the reduced velocity is defined as $U_r = U_\infty/f_n^* D$, where f_n^* is the natural frequency of the stationary cylinder. Hereafter, the asterisk in f is used to denote the value of the stationary cylinder.

Two such equations have to be solved simultaneously for the present case of two side-by-side cylinders. They have to be resolved in a manner that would reflect the strong coupling between the fluid flow and the cylinder dynamics. This

aspect will be discussed in more detail in the following section. Here, it is sufficient to point out that the solution yields the vibration displacements and the velocity of each cylinder as it responds to the surrounding flow field. The incompressible flow calculation is coupled with the cylinder response through the boundary conditions and $\mathbf{C}_f$, thus allowing the fluid–structure interactions to be adequately resolved at each time step if the flow calculation and (6) are solved in an iterative manner.

3. Mesh shape preservation method

Fluid–structure interaction problems generally involve moving physical domains and dynamic remeshing. For a single structure, remeshing can be easily handled because the coordinate system can be attached to the structure. As a result, the distortion of the mesh is not very severe and the remeshing can be carried out with little or no difficulty. For multiple structures in a cross flow, the problem becomes quite complicated because the coordinate system can no longer be attached to the structures, even for the relatively simple case of two side-by-side cylinders. The motions of the cylinders will squeeze the meshes in the space between the cylinders and, depending on the vibration amplitudes, mesh distortion could become so severe that mesh entanglements would result. When this happens, the finite-element/finite-difference method will no longer be valid. In the present problem, the two side-by-side elastic cylinders are free to vibrate within the flow domain. If numerical simulation of this flow-induced vibration problem were to be carried out satisfactorily even under this most severe condition, the meshes in the space between the cylinders need to retain their shape as much as possible even though their area has changed under the action of the cylinder motions. Therefore, a deforming computational mesh that could retain its shape is required to accommodate the arbitrary motion of the two cylinders.

In the following, the general formulation for the 3-D case is first discussed. The numerical implementation of the mathematical model for the 2-D case with an arrangement of two side-by-side cylinders in a cross flow is outlined next. Finally, the calculation details are briefly described.

3.1. Mathematical model

In general finite-element calculations, the variables in a Cartesian physical space (X, Y, Z, τ) have to be transformed to (ξ, η, ζ, τ) in a computational space (Fig. 2), such that

$$\xi = \xi(X, Y, Z, \tau),\ \eta = \eta(X, Y, Z, \tau),\ \zeta = \zeta(X, Y, Z, \tau). \tag{7a–c}$$

The determinant of the Jacobian of the transformation is given by

$$J = \frac{\partial(X, Y, Z)}{\partial(\xi, \eta, \zeta)} = \begin{bmatrix} \dfrac{\partial X}{\partial \xi} & \dfrac{\partial Y}{\partial \xi} & \dfrac{\partial Z}{\partial \xi} \\ \dfrac{\partial X}{\partial \eta} & \dfrac{\partial Y}{\partial \eta} & \dfrac{\partial Z}{\partial \eta} \\ \dfrac{\partial X}{\partial \zeta} & \dfrac{\partial Y}{\partial \zeta} & \dfrac{\partial Z}{\partial \zeta} \end{bmatrix}. \tag{8}$$

A necessary and sufficient condition for the transformation to be valid is that the determinant of the Jacobian J be nonnegative at every point (ξ, η, ζ). Geometrically, J represents the ratio of an elemental volume in the physical space to

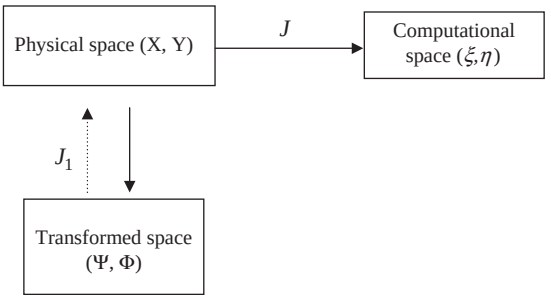

Fig. 2. Relation between the physical, transformed and computational space.

the corresponding volume in the transformed space, or

$$\mathrm{d}V = \mathrm{d}X\,\mathrm{d}Y\,\mathrm{d}Z = J\,\mathrm{d}\xi\,\mathrm{d}\eta\,\mathrm{d}\zeta. \tag{9}$$

If J is to remain finite, the interior angles of the elemental volume should not be too small or too large. Otherwise, J will become very small and the calculation accuracy is significantly affected.

In the finite-element calculations, the surfaces of the cylinders are adjusted according to the motion of the cylinders by means of nodal displacement (Liu et al., 2001). Consequently, when two cylinders attract each other, the meshes between the cylinders are squeezed severely and mesh distortion and mesh entanglements could result. In order to reduce mesh distortion, one way is to preserve the element shape but not the elemental volume. This could be achieved by defining an orthogonal transformed space (Ψ, Φ, Ω) that relates to the (X, Y, Z) physical space through the Laplacian equations,

$$\nabla^2\Psi = \frac{\partial^2\Psi}{\partial X^2} + \frac{\partial^2\Psi}{\partial Y^2} + \frac{\partial^2\Psi}{\partial Z^2} = 0, \tag{10a}$$

$$\nabla^2\Phi = \frac{\partial^2\Phi}{\partial X^2} + \frac{\partial^2\Phi}{\partial Y^2} + \frac{\partial^2\Phi}{\partial Z^2} = 0, \tag{10b}$$

$$\nabla^2\Omega = \frac{\partial^2\Omega}{\partial X^2} + \frac{\partial^2\Omega}{\partial Y^2} + \frac{\partial^2\Omega}{\partial Z^2} = 0, \tag{10c}$$

with appropriate time-independent boundary conditions (Fig. 2). If the (Ψ, Φ, Ω) nodal coordinates can be made independent of time during mesh moving, i.e., the (Ψ, Φ, Ω) value at each element node remains constant even though the coordinates (X, Y, Z) change, then the (Ψ, Φ, Ω) space is always orthogonal. Thus, the element shapes or the interior angles are preserved in the (X, Y, Z) space even though the elemental volume varies in the (X, Y, Z) space (Hui et al., 1999). These conditions can be written in terms of $\Psi = \Psi$ (X, Y, Z), $\Phi = \Phi$ (X, Y, Z) and $\Omega = \Omega$ (X, Y, Z) as

$$\nabla\Psi\cdot\nabla\Phi = \nabla\Phi\cdot\nabla\Omega = \nabla\Psi\cdot\nabla\Omega = 0, \tag{11a}$$

$$\frac{\mathrm{d}\Psi}{\mathrm{d}\tau} = \frac{\mathrm{d}\Phi}{\mathrm{d}\tau} = \frac{\mathrm{d}\Omega}{\mathrm{d}\tau} = 0. \tag{11b}$$

It then follows that

$$\mathrm{d}\Psi = \frac{\partial\Psi}{\partial X}\mathrm{d}X + \frac{\partial\Psi}{\partial Y}\mathrm{d}Y + \frac{\partial\Psi}{\partial Z}\mathrm{d}Z, \tag{12a}$$

$$\mathrm{d}\Phi = \frac{\partial\Phi}{\partial X}\mathrm{d}X + \frac{\partial\Phi}{\partial Y}\mathrm{d}Y + \frac{\partial\Phi}{\partial Z}\mathrm{d}Z, \tag{12b}$$

$$\mathrm{d}\Omega = \frac{\partial\Omega}{\partial X}\mathrm{d}X + \frac{\partial\Omega}{\partial Y}\mathrm{d}Y + \frac{\partial\Omega}{\partial Z}\mathrm{d}Z. \tag{12c}$$

The Jacobian for the transformation from the (X, Y, Z) space to the (Ψ, Φ, Ω) space is

$$J_1 = \frac{\partial(X,Y,Z)}{\partial(\Psi,\Phi,\Omega)} = \begin{bmatrix} \dfrac{\partial X}{\partial\Psi} & \dfrac{\partial Y}{\partial\Psi} & \dfrac{\partial Z}{\partial\Psi} \\ \dfrac{\partial X}{\partial\Phi} & \dfrac{\partial Y}{\partial\Phi} & \dfrac{\partial Z}{\partial\Phi} \\ \dfrac{\partial X}{\partial\Omega} & \dfrac{\partial Y}{\partial\Omega} & \dfrac{\partial Z}{\partial\Omega} \end{bmatrix}. \tag{13}$$

Therefore, when the mesh is remapped in the (X, Y, Z) space, the element shape in the (X, Y, Z) space is preserved even though the element area in the (X, Y, Z) space may change significantly as long as it satisfies

$$\begin{bmatrix} \mathrm{d}\Psi \\ \mathrm{d}\Phi \\ \mathrm{d}\Omega \end{bmatrix} = J_1^{-1}\begin{bmatrix} \mathrm{d}X \\ \mathrm{d}Y \\ \mathrm{d}Z \end{bmatrix} = \begin{bmatrix} \dfrac{\partial\Psi}{\partial X} & \dfrac{\partial\Psi}{\partial Y} & \dfrac{\partial\Psi}{\partial Z} \\ \dfrac{\partial\Phi}{\partial X} & \dfrac{\partial\Phi}{\partial Y} & \dfrac{\partial\Phi}{\partial Z} \\ \dfrac{\partial\Omega}{\partial X} & \dfrac{\partial\Omega}{\partial Y} & \dfrac{\partial\Omega}{\partial Z} \end{bmatrix}\begin{bmatrix} \mathrm{d}X \\ \mathrm{d}Y \\ \mathrm{d}Z \end{bmatrix} = 0. \tag{14}$$

Once this condition is met, the transformation back to (X, Y, Z) and then to the computational space allow the calculations to be carried out with a mesh where the grid angles are preserved. The relation between the transformations is shown in Fig. 2.

3.2. Numerical implementation

The numerical implementation of the mathematical model is now discussed. This is specified to the sample problem considered here, namely, two side-by-side cylinders in a 2-D cross flow. At each time step, the displacement vector of the cylinder, represented by $\boldsymbol{Z}(X,Y)$, is calculated using (6). In order to distribute uniformly the nodal displacement of the cylinder surface throughout the physical domain between the ith and the $(i+1)$th time step, a Laplacian equation of displacement at each node is solved throughout the physical domain with the displacements of the cylinders as the

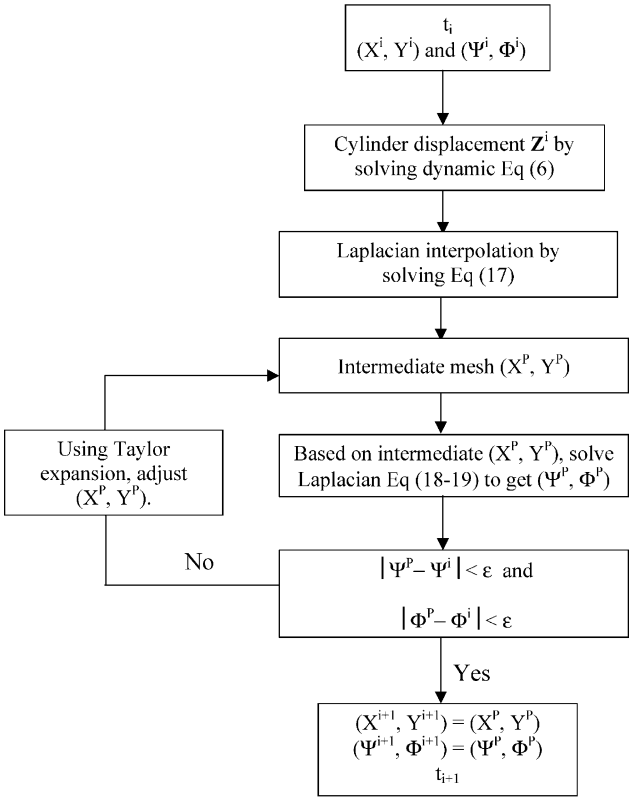

Fig. 3. Flow diagram illustrating the implementation of the mesh preservation technique.

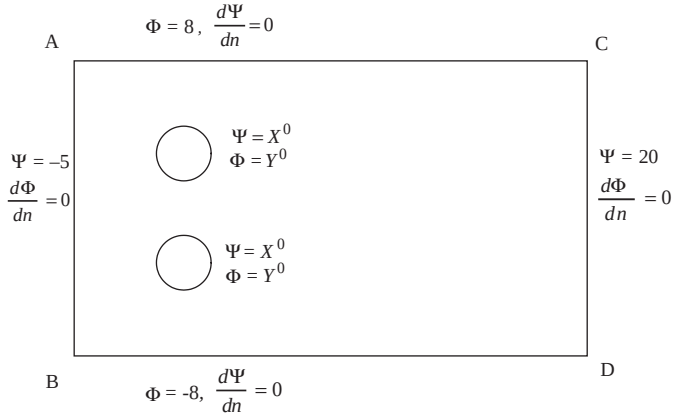

Fig. 4. Boundary conditions specified for the domain in the transformed space.

boundary conditions. The Laplacian equation is

$$\nabla^2 \boldsymbol{\delta} = 0, \tag{15}$$

and the boundary conditions are specified as $\boldsymbol{\delta} = 0$ at the outside boundary and $\boldsymbol{\delta}_i = \boldsymbol{Z}_i$ at each cylinder wall. The entire computational mesh is adjusted by a Laplacian interpolation, which is designed to map the current mesh onto an intermediate mesh (X^P, Y^P), specified by the displacements of the elastic cylinders. This intermediate mesh is placed between the ith and the $(i+1)$th time step (Fig. 3). The superscript P is used to denote the variables in this intermediate mesh. Based on this mesh, the intermediate (Ψ^P, Φ^P) space can be determined by solving (10a) and (10b). Then the intermediate mesh is adjusted to satisfy (14), and this shape-preserved mesh is used for the calculation at the next time step.

The task in this moving mesh scheme is to find $\mathbf{X}^{n+1} = \mathbf{X}^{n+1}(X, Y)$ at the $(i+1)$ time step from $\mathbf{X}^n$ at the i time step (Fig. 3) with the stipulation that the new mesh satisfies (14). In the physical domain $\boldsymbol{\Sigma}(\tau)$, the four boundaries, $\overline{AB}$, $\overline{BC}$, $\overline{CD}$ and $\overline{AD}$, are orthogonal to each other, as shown in Fig. 4. Therefore, the Laplacian equations (10a) and (10b) take on the following boundary conditions; $\Psi = -5$ on $\overline{AD}$, $\Psi = 20$ on $\overline{BC}$, $\nabla\Psi \cdot \mathbf{n} = 0$ on $\overline{AB}$ and $\overline{CD}$, $\Psi =$ initial X coordinates on the cylinder surface for (10a) and $\Phi = -8$ on $\overline{AB}$, $\Phi = 8$ on $\overline{CD}$, $\nabla\Phi \cdot \mathbf{n} = 0$ on $\overline{AD}$ and $\overline{BC}$, $\Phi =$ initial Y coordinates on the cylinder surface for (10b). For simplicity, the boundary value on $\overline{AB}$, $\overline{BC}$, $\overline{CD}$ and $\overline{AD}$ is taken to be the (X, Y) coordinates, but they can be any value theoretically.

The boundary condition on the cylinder surfaces is the most crucial, and its value should remain constant at all time. Eq. (14) can be rewritten as

$$\Psi^{n+1}(\mathbf{X}^{n+1}) = \Psi^n(\mathbf{X}^n) + \nabla\Psi \cdot (\mathbf{X}^{n+1} - \mathbf{X}^n), \tag{16}$$

$$\Phi^{n+1}(\mathbf{X}^{n+1}) = \Phi^n(\mathbf{X}^n) + \nabla\Phi \cdot (\mathbf{X}^{n+1} - \mathbf{X}^n). \tag{17}$$

However, from (16) and (17), $\mathbf{X}^{n+1}$ cannot be determined directly. Therefore, an iterative procedure is required. Using Taylor expansion, the following expressions for Ψ and Φ can be written down:

$$\Psi^{n+1}(\mathbf{X}^{n+1}) \approx \Psi^P(\mathbf{X}^P) + \nabla\Psi^P \cdot (\tilde{\mathbf{X}}^{n+1} - \mathbf{X}^P), \tag{18}$$

$$\Phi^{n+1}(\mathbf{X}^{n+1}) \approx \Phi^P(\mathbf{X}^P) + \nabla\Phi^P \cdot (\tilde{\mathbf{X}}^{n+1} - \mathbf{X}^P). \tag{19}$$

where $\tilde{\mathbf{X}}^{n+1}$ is the target location, and $\tilde{\mathbf{X}}^{n+1} \to \mathbf{X}^{n+1}$. Since the (Ψ, Φ) space is time independent, it follows that

$$\Psi^{n+1}(\mathbf{X}^{n+1}) = \Psi^n(\mathbf{X}^n), \tag{20}$$

$$\Phi^{n+1}(\mathbf{X}^{n+1}) = \Phi^n(\mathbf{X}^n). \tag{21}$$

Thus, the Taylor expansion of (16) and (17) can be reduced to

$$\Psi^n(\mathbf{X}^n) - \Psi^P(\mathbf{X}^P) \approx \nabla\Psi^P \cdot (\tilde{\mathbf{X}}^{n+1} - \mathbf{X}^P), \tag{22}$$

$$\Phi^n(\mathbf{X}^n) - \Phi^P(\mathbf{X}^P) \approx \nabla\Phi^P \cdot (\tilde{\mathbf{X}}^{n+1} - \mathbf{X}^P). \tag{23}$$

From (22) and (23), $\tilde{\mathbf{X}}^{n+1}$ can be determined. However, (22) and (23) are only approximations, the new values of $\tilde{\Psi}^{n+1}$ and $\tilde{\Phi}^{n+1}$ at the new location $\tilde{\mathbf{X}}^{n+1}$ are still not equal to Ψ^n and Φ^n, but much closer than Ψ^P and Φ^P were. Therefore, an iterative procedure of (22) and (23) is required to achieve the final target where $\tilde{\Psi}^{n+1} = \Psi^n$ and $\tilde{\Phi}^{n+1} = \Phi^n$. This procedure of iterating for $\tilde{\mathbf{X}}^{n+1}$ is illustrated in Fig. 3.

Since $\tilde{\mathbf{X}}^{n+1}$ is not a nodal point of the intermediate mesh any more after being moved from $\mathbf{X}^P$, the values of $\tilde{\Psi}^{n+1}$ and $\tilde{\Phi}^{n+1}$ at $\tilde{\mathbf{X}}^{n+1}$ are not readily known. Actually $\tilde{\mathbf{X}}^{n+1}$ may not necessarily be within the same mesh. In order to find $\tilde{\Psi}^{n+1}$ and $\tilde{\Phi}^{n+1}$, a new intermediate mesh is formed based on the new locations of $\tilde{\mathbf{X}}^{n+1}$ (Fig. 3). The Laplacian equations (10a) and (10b) are then solved for the (Ψ, Φ) field on the new intermediate mesh. Using the new intermediate mesh and the new solutions of (Ψ, Φ) the above procedure of adjustment can be repeated until a preset tolerance of $\Psi^n - \tilde{\Psi}^{n+1}$ and $\Phi^n - \tilde{\Phi}^{n+1}$ is met. In this study, the iterative process takes only two to three iterations before the norm of $\Psi^n - \tilde{\Psi}^{n+1}$ and $\Phi^n - \tilde{\Phi}^{n+1}$ for all nodes goes to below 10^{-5}.

3.3. Calculation details

During the calculation, the reference frame is fixed at the far field; i.e., the cylinders are free to vibrate within the calculation domain. At each time step, the fluid flow is solved using the finite-element method. The force on each cylinder is calculated by integrating the pressure and the wall shear stress on the surface. This is then taken as the force

input to (6) and the response of each cylinder is calculated by solving (6) using the Runge–Kutta method. Each cylinder is moved according to the displacement, the mesh is adjusted to preserve the grid angle, and the mesh is remapped according to the mesh adjustment and cylinder motion. The flow field is solved again using the cylinder velocity as the boundary condition. Finally, the whole process is repeated in an iterative way so that the interactions between the fluid and the cylinders are accounted for properly.

The question of grid independence has been investigated by So et al. (2001) for a single cylinder and Liu et al. (2001) for two side-by-side cylinders. They found that, in general, a fine mesh is needed near the cylinder surface. The final number of panels, nodes and elements is as specified in Section 2.1. With this mesh, the calculated mean C_D is mesh-convergent to within 0.5%. Using the mesh adjustment technique, the original shape of the mesh element is preserved very well. Details of mesh adjustment and its possible effects on the calculated vortex-induced forces are discussed in the following sections.

4. Examples on rigid cylinders

In order to demonstrate the effect of mesh deformation on the calculated lift and drag force, two examples of unidirectional laminar flow past rigid cylinders are considered; one a single cylinder, the other a pair of side-by-side cylinders in a cross flow. The flow around the cylinders and the resulting forces are calculated using an undeformed mesh and a distorted mesh. The undeformed mesh is generated using Fastflo (Stokes, 1994) in the same manner as So et al. (2001) and Liu et al. (2001) have done in their calculations. For the single cylinder case, the deformed mesh is generated by initially placing the cylinder at $1.2D$ below the calculation domain symmetry line and then moved to the symmetry line to deform the mesh. Once deformed, the mesh remains unchanged because the cylinder has no motion in this case. The calculations are then carried out using this deformed mesh. For the case of two side-by-side cylinders, the undeformed mesh is again generated using Fastflo by specifying $T/D = 3.0$. The deformed mesh is generated by placing the two cylinders initially at $T/D = 5$ and then move towards each other to give a $T/D = 3$. Thus, the mesh between the cylinders is squeezed and will give rise to a deformed mesh much like that found in the single cylinder case. Again, the deformed mesh remains unchanged in the course of the calculations. The Re for these calculations is chosen at 200. At this Re, the wake flow is still laminar so there is no question of the effect of transition to turbulence. The computational domain is a $25D \times 10D$ rectangular region, the upstream length is about $5D$, while the downstream length is $20D$, and the cylinders are symmetric about the center-line.

4.1. Single cylinder result

For a single cylinder in a cross flow at $\mathrm{Re} = 200$, Roshko (1961) reported a mean drag coefficient, $\bar{C}_D = 1.38$, and a Strouhal number, $\mathrm{St} = 0.18$. Other measurements on vortex shedding give a range for St from 0.17 to 0.196 (Roshko, 1954; Williamson, 1991). This problem has also been simulated by a number of researchers using a variety of numerical methods, ranging from random-vortex method to finite-volume method. Some of the more notable simulations are given by Braza et al. (1986), Borthwick (1986), Franke et al. (1990), Rogers and Kwak (1990), Sa and Chang (1991), Li et al. (1991), Stansby and Slaouti (1993), Zhang and Dalton (1997), Zhou et al. (1999), Farrant et al. (2001) and Meneghini et al. (2001). These calculations give a value for $\bar{C}_D$ that varies from a low of 1.02 to a high of 1.476. Since calculations tend to over-predict $\bar{C}_D$ by about 5% and the measured value reported by Roshko (1961) is 1.38, the predicted value of 1.476 is quite reasonable. In terms of St, the predicted value ranges from a low of 0.162 to a high of 0.200. Thus, the predicted range is larger than the measured range. Therefore, in attempting a comparison between the present calculations with and without a deformed mesh, these variations should be borne in mind. Another point to note is the different t the calculation is carried forward to. Failure to achieve true stationarity in the predicted variables could have contributed to the differences observed in the reported predictions.

The undeformed and deformed mesh chosen for this problem is shown in Fig. 5a and b, respectively. Even though the triangular mesh is unstructured, the grid is nearly symmetric about the cylinder. The enlargements of the undeformed and deformed mesh are shown in Figs. 5c and d, respectively. It can be seen that the mesh closest to the cylinder surface is deformed the most and the vertical height in the closest mesh is compressed by more than 80%. The calculated $\bar{C}_D$ from the undeformed and the deformed mesh are compared in Table 1 together with some of the more reliable measured and predicted results found in the literature. Present $\bar{C}_D$ calculations are closer to the measured value and so is the predicted St. In general, the deformed mesh gives rise to slightly smaller calculated results, particularly for the root mean square lift and drag coefficients, C_D' and C_L', respectively. Their difference is within the range reported for the different numerical simulations. However, the calculated results from the undeformed and deformed mesh are quite consistent and the differences noted are real because the same numerical technique has been used to obtain the results.

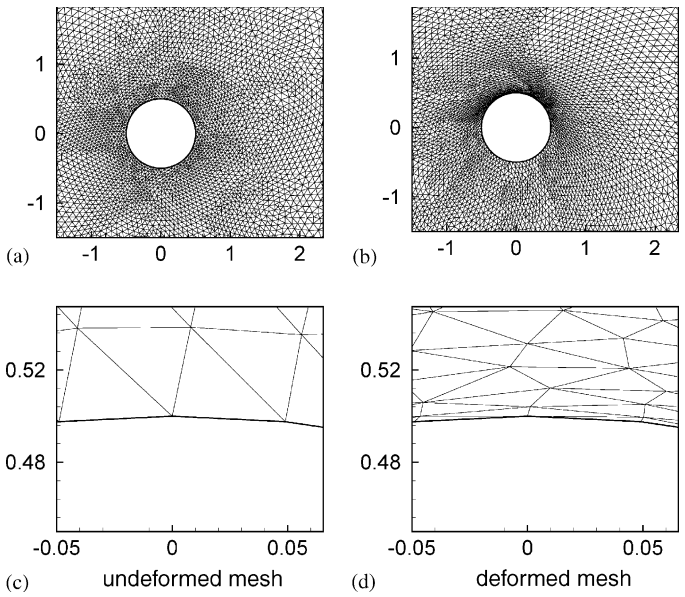

Fig. 5. Undeformed and deformed grid comparison for one rigid cylinder in a cross flow.

Table 1
Comparison of calculated results obtained using a undeformed mesh and a deformed mesh with measurement for a single rigid cylinder at Re = 200

	$\bar{C}_D$	C'_D	C'_L	St
Measurement (Roshko, 1954)	—	—	—	0.17–0.19
Measurement (Roshko, 1961)	1.38	—	—	0.18
Measurement (Williamson, 1991)	—	—	—	0.196
Finite-difference method (Borthwick, 1986)	1.02	—	—	0.188
Finite volume method (Braza et al., 1986)	1.35	—	0.54	0.200
Finite volume method (Franke et al., 1990)	1.31	—	—	0.194
Upwind difference scheme (Rogers and Kwak, 1990)	1.29	—	0.46	0.185
Finite-difference method (Sa and Chang, 1991)	1.13	—	—	0.186
Finite-element method (Li et al., 1991)	1.17	—	0.35	0.180
Random vortex method (Stansby and Slaouti, 1993)	1.317	—	0.248	0.166
Finite-difference method (Zhang and Dalton, 1997)	1.25	—	—	0.196
Vortex-in-cell method (Zhou et al., 1999)	1.476	—	0.219	0.162
Boundary element method (Farrant et al., 2001)	1.36	—	0.50	—
Finite-element method (Meneghini et al., 2001)	1.30	—	0.47	0.196
Present method with undeformed mesh	1.333	0.027	0.431	0.180
Present method with deformed mesh	1.309	0.024	0.404	0.178
Undeformed and deformed mesh difference (%)	1.85	12.9	6.3	1.28

The only difference is in the structure of the mesh. This result essentially verifies the speculation that the effect of mesh distortion on the calculated forces is not very significant in the case of a single cylinder, because the deformed mesh is chosen to represent its motion with vibration amplitude of $1.2D$.

4.2. Two side-by-side cylinders

No reliable measurements for the case where Re = 200 and $T/D = 3.0$ can be found in the literature. However, a few calculations at the same conditions are available. Among the more recent ones are the random vortex simulation study of Slaouti and Stansby (1992) and the finite-element calculation of Meneghini et al. (2001). These calculations show that

Table 2
Comparison of the calculated results for two side-by-side rigid cylinders at Re = 200 and $T/D = 3.0$ with other results

	Slaouti and Stansby (1992)	Meneghini et al. (2001)	With undeformed grid	With deformed grid
$\bar{C}_{D1}$	1.23	1.41	1.076	1.057
C'_{D1}	0.11	—	0.019	0.016
$\bar{C}_{D2}$	1.22	1.41	1.077	1.046
C'_{D2}	0.07	—	0.017	0.017
$\bar{C}_{L1}$	0.14	0.10	0.114	0.129
C'_{L1}	0.71	—	0.202	0.196
$\bar{C}_{L2}$	0.00	−0.10	−0.111	−0.135
C'_{L2}	0.64	—	0.200	0.177
f_{s1}	0.215	0.200	0.192	0.193
f_{s2}	0.215	0.200	0.192	0.193

there are two distinct wakes behind the cylinders and that the vortex-shedding frequencies from the two cylinders are essentially identical. This case has also been calculated by Liu et al. (2001). Their results compared well with those reported by Slaouti and Stansby (1992), except for the root mean square fluctuating forces. The present comparison is made with these three cases using a deformed mesh generated by first putting the cylinders at $T/D = 5$ and then moving them towards each other until $T/D = 3.0$. Thus, the grid between the cylinders is squeezed by about 80%. From this point on, the subscripts 1 and 2 are used to denote cylinders 1 and 2, respectively, as indicated in Fig. 1. All the results are tabulated in Table 2 for comparison. It should be pointed out that the results reported by Slaouti and Stansby (1992) and Meneghini et al. (2001) are calculated to $\tau = 200$, while the present results are calculated to $\tau = 1000$.

In this case, there are two distinct vortex streets and the vortex-shedding frequencies are essentially identical. All three calculations give this behavior; however, the predicted shedding frequency varies from a low of 0.19, given by the present calculations, to a high of 0.215, given by Slaouti and Stansby (1992). Similarly, the prediction of $\bar{C}_D$ also varies from a low of about 1 to a high of 1.41. These differences could be due to the fact that the signals are not quite stationary for the cases reported by Slaouti and Stansby (1992) and Meneghini et al. (2001). As a result, their calculated $\bar{C}_D$ could include the contribution of the transient behavior of the developing wake flow. In the previous results reported by Liu et al. (2001), the calculations were only carried out to $\tau = 500$. However, it was found that the force and displacement signals were not exactly stationary at $\tau = 500$. Therefore, their calculations were repeated and carried out to $\tau = 1000$ to achieve a stationary state for all relevant quantities. The results thus obtained are slightly different from those reported earlier by Liu et al. (2001). As shown in the single cylinder case, the present finite element method gives a predicted $\bar{C}_D$ that is lower than that given by a vortex method (Zhou et al., 1999). Similarly, this is also observed in the case of two side-by-side cylinders. Unlike the single cylinder case, the highest value is predicted by the finite-element method of Meneghini et al. (2001). The present method and that of Meneghini et al. (2001) replicated the repelling behavior correctly. It is obvious that the vortex method (Slaouti and Stansby, 1992) fails to predict this behavior. The undeformed grid results, other than $\bar{C}_L$ and f_s, are slightly higher than those deduced from the deformed grid. It should be pointed out that the values of the predicted C'_D given by the present method using the undeformed and deformed grid are approximately equal, and they differ substantially from the predictions of Slaouti and Stansby (1992). Whether these predictions are correct remains to be verified. The fact of the matter is that the undeformed and deformed grids give different results, especially those of $\bar{C}_D$ and $\bar{C}_L$.

5. Two elastic cylinders in a cross flow

Having studied the effect of mesh distortion on the calculated vortex-induced forces on a single cylinder and two side-by-side cylinders in a cross flow, the next step is to examine this effect in the case where fluid–structure interaction plays an important role in the whole problem. Liu et al. (2001) have investigated the case of two freely vibrating cylinders in a cross flow with the cylinders arranged side-by-side and Re = 200. Three different mass ratios were studied, ranging from $M_r = 7$ to 66. In Liu et al.'s (2001) calculations, the parameters T/D, M_r, U_r and ζ_s were chosen so that the cylinders will not vibrate to the extent that they would touch each other when T/D, M_r and ζ_s were smallest. With a combination of $T/D = 3.0$, $M_r = 10$, $U_r = 5$ and $M_r\zeta_s = 0.3$, Liu et al. (2001) found that the peak-to-peak transverse amplitude of vibration of the cylinders is slightly less than $1D$. In other words, at an instant when the cylinders moved towards each other, the gap between the cylinders was reduced from $2D$ to $1D$ and the mesh was squeezed by at least 50%. In some cases, the

mesh was squeezed by more than 80%. The squeezing of the mesh was also found when the cylinders moved away from each other, but it occurred on the free stream side rather than in the gap. For this case, vortex shedding is anti-phase. This behavior was found irrespective whether the cylinders were moving away or towards each other. As a result, two parallel vortex streets were formed in the wake of the two side-by-side cylinders. Currently, there are no data available to verify this simulation (Liu et al., 2001). However, this case gives rise to severe mesh distortion, so it could be used as an example to test the effectiveness of the mesh shape preservation method.

The undeformed grid for this case is again generated using Fastflo and grid distortion is allowed when the mesh shape preservation method is not invoked. Thus, this calculation is the same as that carried out by Liu et al. (2001). When the mesh shape preservation method is employed the distorted grid is transformed to give a mesh whose shape is preserved. The resulting grid for the former case where the grid is allowed to deform and the latter case where the mesh shape is preserved are plotted in the same figures. In each figure, there are six panels. The top two panels show the original mesh, the middle two panels depict the mesh without the preservation method applied while the bottom two panels the mesh with the preservation method applied. The instant when the two cylinders are at their maximum separation is shown in Fig. 6, while Fig. 7 shows the instant when they are at their minimum separation. Mesh deformation can be estimated for both situations; it is about 83% for the case shown in Fig. 6 and about 20% for Fig. 7. It is clear that the method is able to restore the grid to its original shape but not the area of the mesh elements. The mesh shape preservation and the calculation are carried out with full fluid cylinder coupling, in order to account for fluid–structure interactions properly.

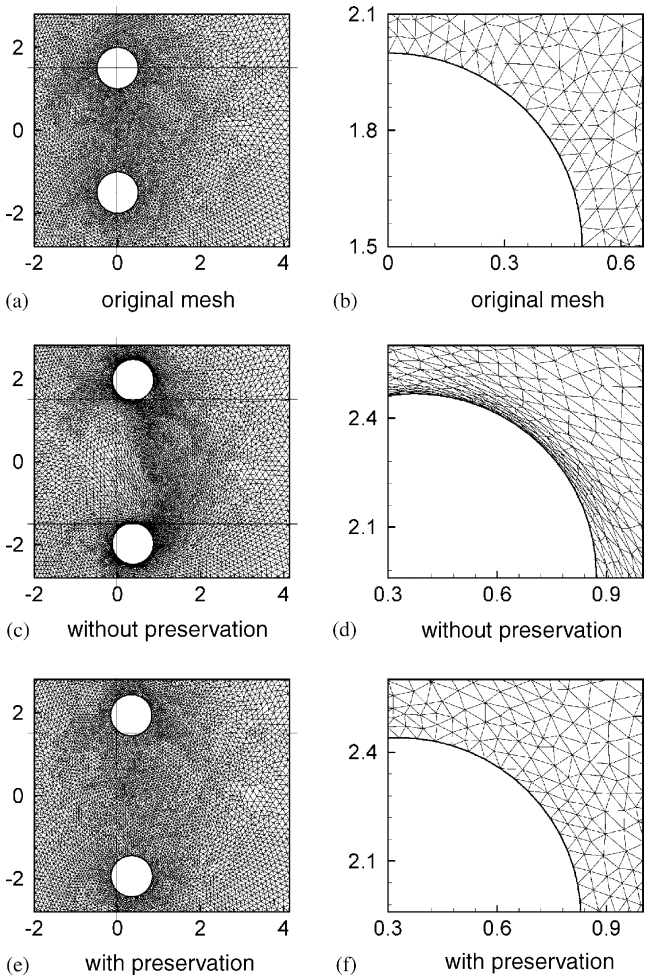

Fig. 6. Grid distribution with and without mesh shape preservation for two elastic cylinders ($M_r = 10$) in a cross flow at an instant when they are furthest away from each other.

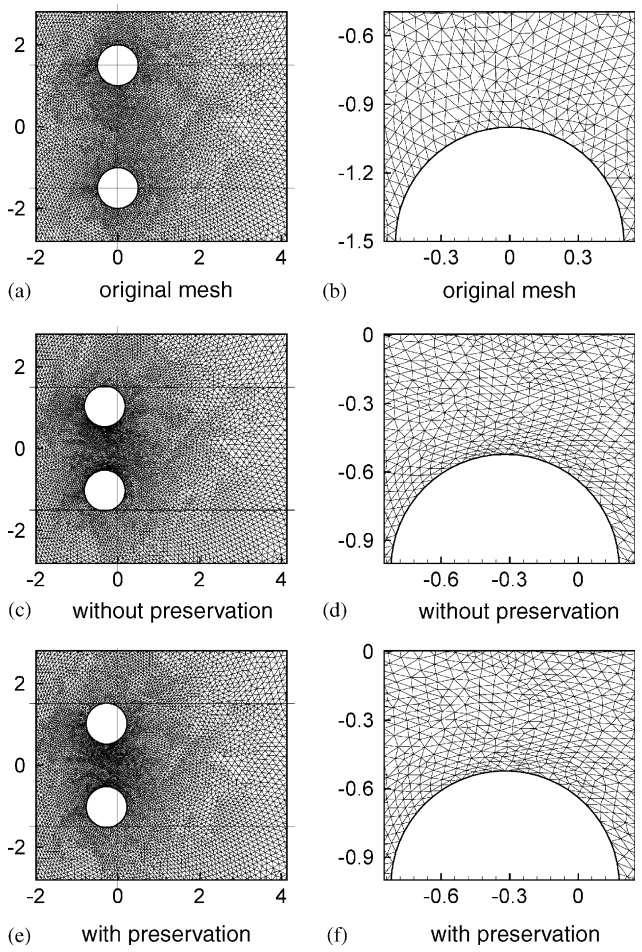

Fig. 7. Grid distribution with and without mesh shape preservation for two elastic cylinders ($M_r = 10$) in a cross flow at an instant when they are closest to each other.

The calculated statistics of the vortex-induced forces and displacements are tabulated in Table 3 for comparison. There are significant differences between those values obtained with and without mesh shape preservation. In general, the values deduced with mesh shape preservation are higher than those without. This is especially true for cylinder 2, where the difference in $\bar{C}_{L2}$ and $\bar{Y}_2$ between the two sets of values is as large as 25%, even though the values themselves are quite small. The difference in C'_{D1} and X'_1 is also quite substantial, greater than 10%. Presently, there are no measurements to verify the correctness of these values. However, the effectiveness of the mesh shape preservation method is clearly shown in this calculation.

The time series of C_D, C_L, X and Y for the two cylinders are shown in Figs. 8–11, respectively. It is clear from the time series that stationarity has been achieved as early as $\tau = 200$. There is no time lag between the two sets of signals; thus indicating that the shedding frequency deduced from these signals is essentially the same (Table 3). In general, the signals deduced from the case where the mesh shape preservation technique has been used have slightly higher peaks. This explains why the calculated statistics are larger. To further verify that the shedding frequency deduced with and without mesh shape preservation is the same a sample spectral density of Y_1 is compared in Fig. 12. It can be seen that the shedding frequency deduced from the two methods is the same. However, there is a slight difference in the spectral density resulting from the difference in cylinder vibrations.

It is obvious that the distorted grid does not significantly affect the calculated vortex shedding and wake behavior. Only the calculated statistics of the vortex-induced forces and the cylinder displacements are influenced by grid deformation. The present method alleviates grid deformation in the calculations of these variables and could possibly contribute to an improvement on the accuracy of these variables in cases where the flow-induced vibrations are very large.

Table 3
Comparison of the calculated results for two side-by-side elastic cylinders at Re = 200, $T/D = 3.0$, $M_r\zeta_s = 0.3$ and $U_r = 5.0$ obtained with and without mesh preservation

	With mesh preservation (A)	Without mesh preservation (B)	$\frac{B-A}{A} \times 100\%$
$\bar{C}_{D1}$	1.16	1.13	−2.6
C'_{D1}	0.601	0.666	10.8
$\bar{C}_{D2}$	1.16	1.12	−3.6
C'_{D2}	0.628	0.670	6.7
$\bar{C}_{L1}$	0.1716	0.1798	4.8
C'_{L1}	0.676	0.704	4.2
$\bar{C}_{L2}$	−0.1688	−0.2050	21.5
C'_{L2}	0.668	0.724	8.2
$\bar{Y}_1$	0.00489	0.00494	1
$Y_{1\max} - Y_{1\min}$	0.909	0.966	6.27
Y'_1	0.318	0.331	4
$\bar{Y}_2$	−0.00482	−0.00600	24.5
$Y_{2\max} - Y_{2\min}$	0.895	0.969	8.27
Y'_2	0.316	0.340	7.7
$\bar{X}_1$	0.0334	0.0326	−2.4
$X_{1\max} - X_{1\min}$	0.614	0.695	13.19
X'_1	0.214	0.241	12.6
$\bar{X}_2$	0.0335	0.0320	-4.5
$X_{2\max} - X_{2\min}$	0.657	0.697	2.63
X'_2	0.227	0.243	7
f_{s1}	0.1996	0.1996	0
f_{s2}	0.1996	0.1996	0

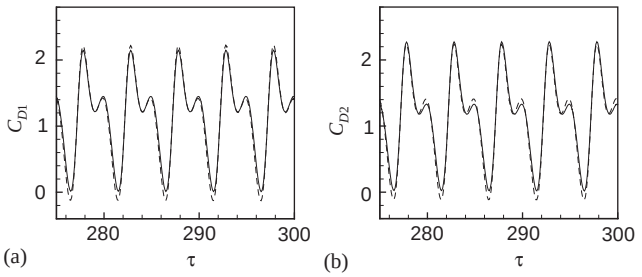

Fig. 8. Comparison of the drag coefficient between the case with and without mesh shape preservation: - - - - -, without preservation; —, with preservation.

In order to further illustrate the necessity of this mesh preservation method in the calculations of flow-induced vibration problems, M_r was reduced to 7 so that $M_r\tau_s = 0.21$, while keeping all other parameters constant in the two side-by-side elastic cylinders case treated before. In this calculation, it was found that the gap between the two cylinders could be as small as $0.2D$, but the cylinders remained separate and did not touch each other. The transient calculations showing the vibration of the cylinders with and without using the mesh preservation method are plotted in Fig. 13. The left column (Figs. 13a and c) shows the calculated results where the mesh preservation method has been used, while the right column (Figs. 13b and d) the corresponding results obtained without using the method. The time series of the cylinders for each case are plotted in the first row of the figure and the enlarged grids are shown in the bottom row. With the use of the mesh preservation method, it was possible to carry out the calculations to the stationary state. The enlarged grid at the location where the gap was $0.2D$ (Fig. 13c) clearly shows that the mesh shape has been preserved and that is why the calculations can be continued. On the other hand, mesh entanglement occurred when the gap reached $0.5D$ for the calculation where the mesh preservation method has not been used (Fig. 13d). Consequently, the calculation cannot be continued beyond $\tau = 110$. The only difference between this case and the previous one is M_r,

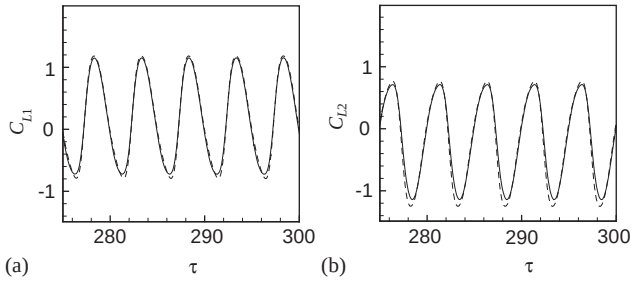

Fig. 9. Comparison of the lift coefficient between the case with and without mesh shape preservation: - - - - -, without preservation; —, with preservation.

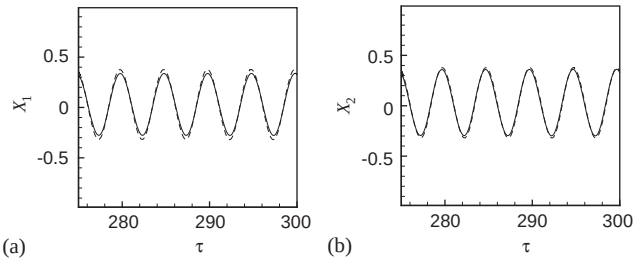

Fig. 10. Comparison of the Y displacement between the case with and without mesh shape preservation: - - - - -, without preservation; —, with preservation.

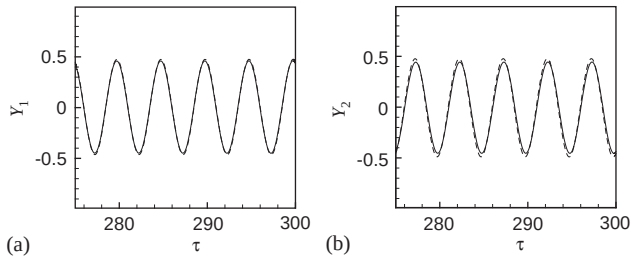

Fig. 11. Comparison of the X displacement between the case with and without mesh shape preservation: - - - - -, without preservation; —, with preservation.

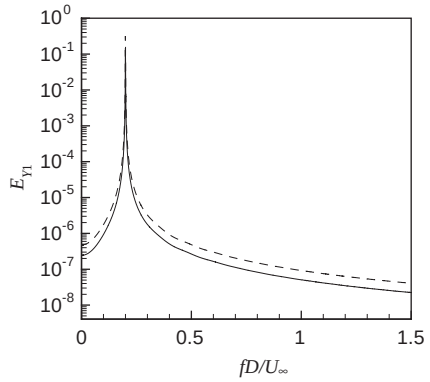

Fig. 12. Comparison of the spectral behavior between the case with and without mesh shape preservation: - - - - -, without preservation; —, with preservation.

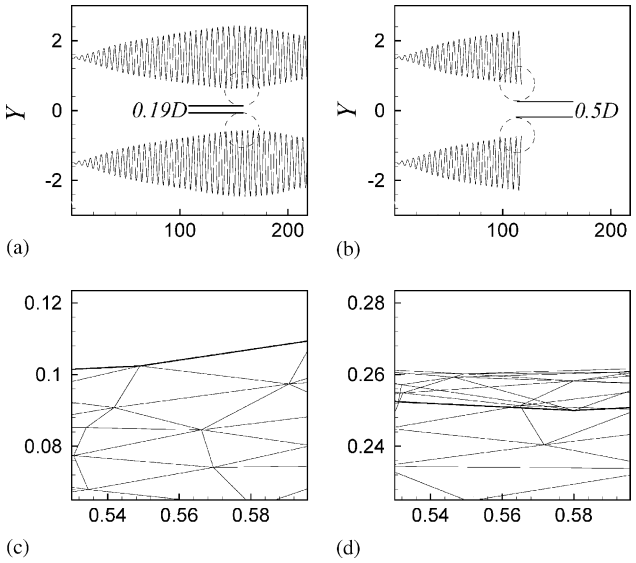

Fig. 13. Grid distribution with and without mesh shape preservation for two elastic cylinders ($M_r = 7$) in a cross flow at the location where the gap is smallest.

which is reduced from 10 to 7. This rather small reduction in M_r is sufficient to clearly demonstrate the merit of the mesh preservation method.

6. Conclusions

In numerical simulations of flow-induced vibration problems with multiple structures in a cross flow; quite often the grid between the structures is severely distorted as a result of large amplitude vibrations of the structures. For some situations, the grid could be so severely deformed that grid entanglement results. When that happens, the finite element/difference method used to resolve the fluid–structure interaction is no longer valid. This paper proposes a method to preserve the mesh shape in the grid but not the area of the mesh. Therefore, the method allows the most severely deformed grid to retain its original shape and hence facilitates continuation of the numerical simulation. The effect of grid distortion on the predicted results of the vortex-induced forces and the structural displacements is first assessed assuming a single rigid cylinder in a cross flow. Then, the method is extended to treat two side-by-side cylinders in a cross flow where the two cylinders are assumed to be rigid as well as elastic. For the rigid cylinder cases, the cylinder or cylinders are moved by about $1D$ to the center-line or towards each other to generate the distorted grid. In the freely vibrating case, the motion of the cylinders distorts the grid at every time step. The mesh shape preservation method when applied to the distorted grid restores the mesh to its original shape but not its original area. Calculations have been carried out with and without invoking the mesh shape preservation method and the calculated statistics of the induced forces and cylinder displacements for cases where $M_r > 7$ are compared. Results show that the difference is quite substantial for certain variables, such as the transverse vibration amplitude and the lift force. However, the distorted grid has little effect on the calculated vortex-shedding frequency of the cylinders. This is true for both rigid and elastic cylinders considered. As M_r was reduced to 7, mesh entanglement occurred if the mesh preservation method was not invoked and the calculation was terminated when the cylinder gap was reduced to $0.5D$. With mesh preservation applied, calculation was possible until cylinder vibrations have reached their stationary state. These results, therefore, show that the mesh shape preservation method is quite valid and necessary for flow-induced vibration problems with severely deformed grids.

Acknowledgements

Support given by the Research Grants Council of the Government of the HKSAR under Grant Nos. PolyU5161/00E and PolyU5166/01E are gratefully acknowledged.

References

Bearman, P.W., 1988. Vortex shedding from oscillating bluff bodies. Annual Review of Fluid Mechanics 16, 195–222.

Bearman, P.W., 1995. Flow-induced vibration. Proceedings of the Sixth International Conference on Flow-Induced Vibration, London, UK, 10–12 April, A.A. Balkema, Rotterdam.

Bearman, P.W., Wadcock, A.J., 1973. The interaction between a pair of circular cylinders normal to a stream. Journal of Fluid Mechanics 61, 499–511.

Borthwick, A., 1986. Comparison between two finite-difference schemes for computing the flow around a cylinder. International Journal for Numerical Methods in Fluids 6, 275.

Braza, M., Chassaing, P., Ha Minh, H., 1986. Numerical study and physical analysis of the pressure and velocity fields in the near wake of a circular cylinder. Journal of Fluid Mechanics 165, 79–130.

Chang, K., Song, C., 1990. Interactive vortex shedding from a pair of circular cylinders in a transverse arrangement. International Journal for Numerical Methods in Fluids 11, 317–329.

Chilukuri, R., 1987. Incompressible laminar flow past a transversely vibrating cylinder. Journal of Fluids Engineering 109, 166–171.

Donea, J., Giuliani, S., Halleux, J.P., 1982. An arbitrary Lagrangian–Eulerian finite element method for transient dynamic fluid–structure interactions. Computational Methods Applied to Mechanical Engineering 33, 689–723.

Duggal, A.S., Niedzwecki, J.M., 1995. Dynamic response of a single flexible cylinder in waves. Journal of Offshore Mechanics and Arctic Engineering 117, 99–104.

Evangelinos, C., Karniadakis, G.E., 1999. Dynamics and flow structures in the turbulent wake of rigid and flexible cylinders subject to vortex-induced vibrations. Journal of Fluid Mechanics 400, 91–124.

Evangelinos, C., Lucor, D., Karniadakis, G.E., 2000. DNS-derived force distribution on flexible cylinders subject to vortex-induced vibration. Journal of Fluids and Structures 14, 429–440.

Farhat, C., Lesoinne, M., Maman, N., 1995. Mixed explicit/implicit time integration of coupled aeroelastic problems: three-field formulation, geometric conservation and distributed solution. International Journal for Numerical Methods in Fluids 21, 807–835.

Farrant, T., Tan, M., Price, W.G., 2001. A cell boundary element method applied to laminar vortex shedding from circular cylinders. Computers and Fluids 30, 211–236.

Franke, R., Rodi, W., Schonung, B., 1990. Numerical calculation of laminar vortex-shedding flow past cylinders. Journal of Wind Engineering and Industrial Aerodynamics 35, 237–257.

Gopalkrishnan, R., Triantafyllou, M.S., Triantafyllou, G.S., Barrett, D., 1994. Active vorticity control in a shear flow using a flapping foil. Journal of Fluid Mechanics 274, 1–21.

Griffin, O.M., Koopmann, G.H., 1977. The vortex-excited lift and reaction forces on resonantly vibrating cylinders. Journal of Sound and Vibration 54, 435–448.

Griffin, O.M., Hall, M.S., 1991. Review—vortex shedding lock-on and flow control in bluff body wakes. Journal of Fluids Engineering 113, 526–534.

Griffin, O.M., Skop, R.A., Koopmann, G.H., 1973. The vortex excited resonant vibrations of circular cylinders. Journal of Sound and Vibration 31, 235–249.

Hirt, C.W., Amsden, A.A., Cook, H.K., 1974. An arbitrary Lagrangian–Eulerian computing method for all flow speeds. Journal of Computational Physics 14, 227–253.

Hui, W.H., Li, P.Y., Li, Z.W., 1999. A unified coordinate system for solving the two-dimensional Euler equations. Journal of Computational Physics 153, 596–637.

Hurlbut, S., Spaulding, M., White, F., 1982. Numerical solution for laminar two-dimensional flow about a cylinder oscillating in a uniform stream. Journal of Fluids Engineering 104, 214–220.

Khalak, A., Williamson, C.H.K., 1996. Dynamics of a hydroelastic cylinder with very low mass and damping. Journal of Fluids and Structures 10, 455–472.

Lecointe, Y., Piquet, Y., 1989. Flow structure in the wake of an oscillating cylinder. Journal of Fluids Engineering 111, 139–148.

Lewis, R.I., 1991. Surface vorticity modelling of separated flows from two-dimensional bluff bodies of arbitrary shape. Journal of Mechanical Engineering Science 23, 1–12.

Li, J., Chambarel, A., Donneaud, M., Martin, R., 1991. Numerical study of laminar flow past one and two circular cylinders. Computers and Fluids 19, 155–170.

Liu, Y., So, R.M.C., Lau, Y.L., Zhou, Y., 2001. Numerical studies of two side-by-side cylinders in a cross flow. Journal of Fluids and Structures 15, 1009–1030.

Mendes, P.A., Branco, F.A., 1999. Analysis of fluid–structure interaction by an arbitrary Lagrangian–Eulerian finite element formulation. International Journal for Numerical Methods in Fluids 30, 897–919.

Meneghini, J.R., Saltara, F., Siqueira, C.L.R., Ferrari Jr., J.A., 2001. Numerical simulation of flow interference between two circular cylinders in tandem and side-by-side arrangements. Journal of Fluids and Structures 15, 327–350.

Mittal, S., Kumar, V., 1999. Finite element study of vortex-induced cross-flow and in-line oscillations of a circular cylinder at low Reynolds numbers. International Journal for Numerical Methods in Fluids 31, 1087–1120.

Mittal, S., Tezduyar, T.E., 1992. A finite element study of incompressible flows past oscillating cylinders and aerofoils. International Journal for Numerical Methods in Fluids 15, 1073–1118.

Newman, D.J., Karniadakis, G., 1997. A direct numerical simulation study of flow past a freely vibrating cable. Journal of Fluid Mechanics 344, 95–136.

Nomura, T., Hughes, T., 1992. An arbitrary Lagrangian–Eulerian finite element method for interaction of fluid and a rigid body. Computational Methods Applied to Mechanical Engineering 95, 115–138.

Obasaju, E.D., Ermshaus, R., Naudascher, E., 1990. Vortex-induced streamwise oscillations of a square-section cylinder in a uniform stream. Journal of Fluid Mechanics 213, 171–189.

Paidoussis, M.P., 1998. . Fluid–Structure Interactions—Slender Structures and Axial Flow, Vol. 1. Academic Press, London.

Ramaswamy, B., Kawahara, M., 1987. Arbitrary Lagrangian–Eulerian finite element method for unsteady, convective, incompressible viscous free surface fluid flow. International Journal for Numerical Methods in Fluids 7, 1053–1075.

Rogers, S.E., Kwak, D., 1990. Upwind differencing scheme for time-accurate incompressible Navier–Stokes equations. AIAA Journal 28, 253–262.

Roshko, A., 1954. On the drag and shedding frequency of two-dimensional bluff bodies. NACA TN3169, *National Advisory Committee for Aeronautics*, Washington.

Roshko, A., 1961. Experiments on the flow past a circular cylinder at very high Reynolds number. Journal of Fluid Mechanics 10, 345–356.

Sa, J.Y., Chang, K.S., 1991. Shedding patterns of the near-wake vortices behind a circular cylinder. International Journal for Numerical Methods in Fluids 12, 463–474.

Sarpkaya, T., 1995. Hydrodynamic damping, flow-induced oscillations, and biharmonic response. Journal of Offshore Mechanics and Arctic Engineering 117, 232–238.

Slaouti, A., Stansby, P.K., 1992. Flow around two circular cylinders by the random-vortex method. Journal of Fluids and Structures 6, 641–670.

So, R.M.C., Savkar, S.D., 1981. Buffeting forces on rigid circular cylinders in cross flows. Journal of Fluid Mechanics 105, 397–425.

So, R.M.C., Zhou, Y., Liu, M.H., 2000. Free vibrations of an elastic cylinder in a cross flow and their effects on the near wake. Experiments in Fluids 29, 130–144.

So, R.M.C., Liu, Y., Chan, S.T., Lam, K., 2001. Numerical studies of a freely vibrating cylinder in a cross flow. Journal of Fluids and Structures 15, 845–866.

Spivack, H.M., 1946. Vortex frequency and flow pattern in the wake of two parallel cylinders at varied spacing normal to an air stream. Journal of Aeronautical Sciences 13, 289–297.

Stansby, P.K., 1981. A numerical study of vortex shedding from one and two circular cylinders. Aeronautical Quarterly 32, 48–71.

Stansby, P.K., Slaouti, A., 1993. Simulation of vortex shedding including blockage by the random-vortex and other methods. International Journal for Numerical Methods in Fluids 17, 1003–1013.

Stokes, N., 1994. Manual of Fastflo, Version 2. CSIRO, Australia.

Sumner, D., Wong, S., Price, S.J., Paidoussis, M.P., 1997. Two and three side-by-side circular cylinders in steady cross flow. Proceedings of the 16th Canadian Congress of Applied Mechanics 1, 273–274.

Sumner, D., Wong, S., Price, S.J., Paidoussis, M.P., 1999. Fluid behavior of side-by-side circular cylinders in steady cross flow. Journal of Fluids and Structures 13, 309–338.

Tezduyar, T.E., Liou, J., Ganjoo, D.K., Behar, M., 1990. Solution techniques for the vorticity-stream function formulation of two-dimensional unsteady incompressible flows. International Journal for Numerical Methods in Fluids 11, 515–539.

Wang, X.Q., So, R.M.C., Liu, Y., 2001. Flow-induced vibration of an Euler–Bernoulli beam. Journal of Sound and Vibration 243, 241–268.

Wei, R., Sekine, A., Shimura, M., 1995. Numerical analysis of 2D vortex-induced oscillations of a circular cylinder. International Journal for Numerical Methods in Fluids 21, 993–1005.

Williamson, C.H.K., 1985. Evolution of a single wake behind a pair of bluff bodies. Journal of Fluid Mechanics 159, 1–18.

Williamson, C.H.K., 1991. 2-D and 3-D aspects of the wake of a cylinder, and their relation to wake computations. In: Anderson, C.R., Greengard, C. (Eds.), Vortex Dynamics and Vortex Methods Vol. 28. Lectures in Applied Mathematics, American Mathematical Society, pp. 719–751.

Williamson, C.H.K., Roshko, A., 1988. Vortex formation in the wake of an oscillating cylinder. Journal of Fluids and Structures 2, 355–381.

Yang, G., Gauson, D.M., Ingram, D.M., Saunders, R., Batten, P., 1997. A Cartesian cut cell method for compressible flows— Part B: moving body problems. Aeronautical Journal 101, 57–65.

Zhang, J., Dalton, C., 1997. Interaction of a steady approach flow and a circular cylinder undergoing forced oscillation. Journal of Fluids Engineering 119, 808–813.

Zhou, C.Y., So, R.M.C., Lam, K., 1999. Vortex-induced vibrations of elastic circular cylinders. Journal of Fluids and Structures 13, 165–189.

Zhou, Y., Wang, Z.J., So, R.M.C., Xu, S.J., Jin, W., 2001. Free vibrations of two side-by-side cylinders in a cross flow. Journal of Fluid Mechanics 443, 197–229.